# Chapter 4: Experimental Investigation

## 4.1. Experimentation

### 4.1.1. Setup Description

The experimental setup for the ORC system comprises three distinct and interconnected loops: the top hot fluid loop, the middle working fluid loop, and the bottom cold fluid loop, each serving to transfer, convert, and reject heat, respectively. The layout of an experimental setup for the organic Rankine cycle is shown in Figure 4.1. In the top hot fluid loop, a heat source supplies thermal energy to the evaporator, achieved using a 3-phase heater system with a temperature controller to simulate waste heat at a specific temperature grade. An RTD provides accurate temperature readings, ensuring a consistent heat supply to the system. Downstream of a gear pump, a pressure sensor monitors fluid pressure to maintain heat transfer efficiency and safety, while an electromagnetic mass flow meter measures the mass flow rate, regulating energy delivery to the system. The middle working fluid loop is the core of the ORC system, incorporating the evaporator, expander, condenser, and pump. A brazed plate heat exchanger functions as the evaporator, while a modified scroll compressor, adapted into a scroll expander, facilitates energy extraction. An in-house fabricated fin-type forced-air condenser handles condensation through forced convection, and a diaphragm pump enables leak-proof, fire-resistant fluid handling to prevent incidents caused by pressure surges. A high-pressure storage tank is designed to safely contain working fluid when the system is idle, preventing leaks and accommodating pressure variations. A critical component, the separator, is placed after the evaporator to divide the vapor and liquid phases of the working fluid, as fluctuations in heating load may result in mixed-phase output from the evaporator. The vaporized fluid proceeds through the scroll expander, where pressure energy is converted into mechanical work, driving a pulley that can connect to an alternator for electricity generation. This loop includes RTDs to track temperature changes at key points evaporator, expander outlet, and condenser while pressure sensors at the evaporator inlet, expander inlet and outlet, and condenser inlet monitor the pressure conditions, crucial for phase changes and cycle efficiency. A mass flow meter ensures precise measurement of the working fluid's flow rate, vital for balanced thermodynamic operation and consistent power output.

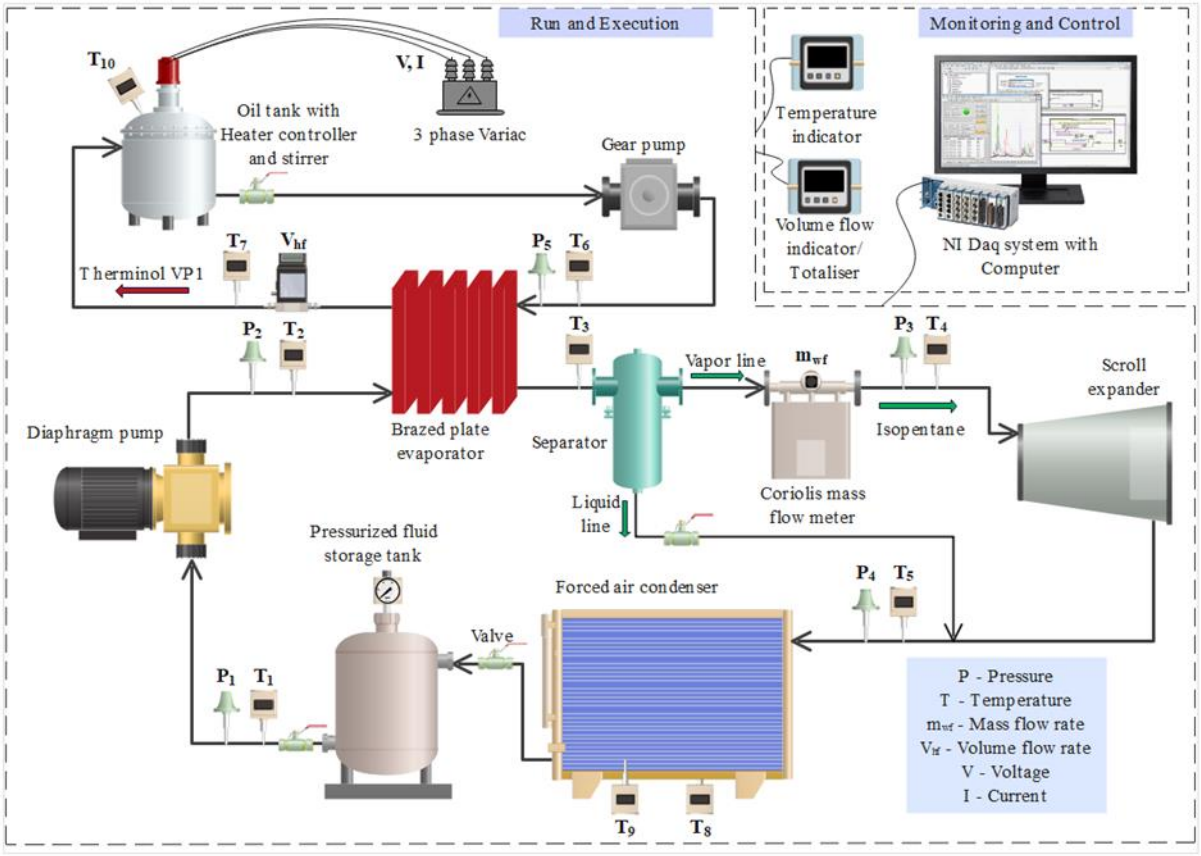


Figure 4.1. Layout of the experimental setup for the Organic Rankine Cycle

Heat is removed from the condenser in the bottom cold fluid (air) loop to achieve the necessary low-temperature conditions for effective condensation. Fan monitors temperatures before and after the condenser, ensuring sufficient heat removal, while a pressure sensor at the cooling fluid outlet provides data for flow regulation to prevent backpressure. Additionally, an air flow meter measures the cold fluid's rate, which is critical for maintaining temperature stability and adequate heat absorption.

#### 4.1.1.1. Fabrication and modification of Equipment's

The fabrication of the vertical separator, as shown in Figure 4.2(a), is designed to efficiently separate liquid and vapor phases using gravity and a demister pad, having 4-inch diameter and 14-inch total height. The separator body is constructed from SS 314, a stainless-steel material known for its corrosion resistance and durability in high-temperature and high-pressure environments, making it suitable for the organic Rankine cycle. The separator consists of three ports. The top port functions as the vapor outlet, allowing separated vapor to exit the system. The middle port is the inlet for the vapor-liquid mixture, positioned so that the incoming flow can enter and begin the separation process. The bottom port serves as the liquid

outlet, enabling the denser liquid phase to drain out after separation. The demister pad, positioned between the two halves of the vertical separator, is constructed from fine chicken mesh wire of 4-inch diameter and 2.5-inch height. This mesh acts as a filter, capturing any remaining liquid droplets in the vapor flow. When the vapor-liquid mixture enters the separator through the middle port, the liquid droplets are trapped by the mesh, while gravity pulls the denser liquid down to the bottom. This demister pad, secured with a metal cross-bracket, enhances the separation efficiency by ensuring that only vapor exits from the top port. The fabrication process involves first shaping and welding the stainless steel components to form a robust vertical cylinder with three distinct ports. After the cylinder body is formed, the demister pad is installed by placing it centrally between the top and bottom sections, ensuring a secure fit to handle the pressure and flow of the incoming mixture. The sections are then bolted together, compressing the demister pad and creating a gasket seal that prevents leakage. This separator setup allows gravity and the demister pad to work in tandem, ensuring effective separation of liquid and vapor phases, which is essential for maintaining system efficiency in the ORC experimental setup.

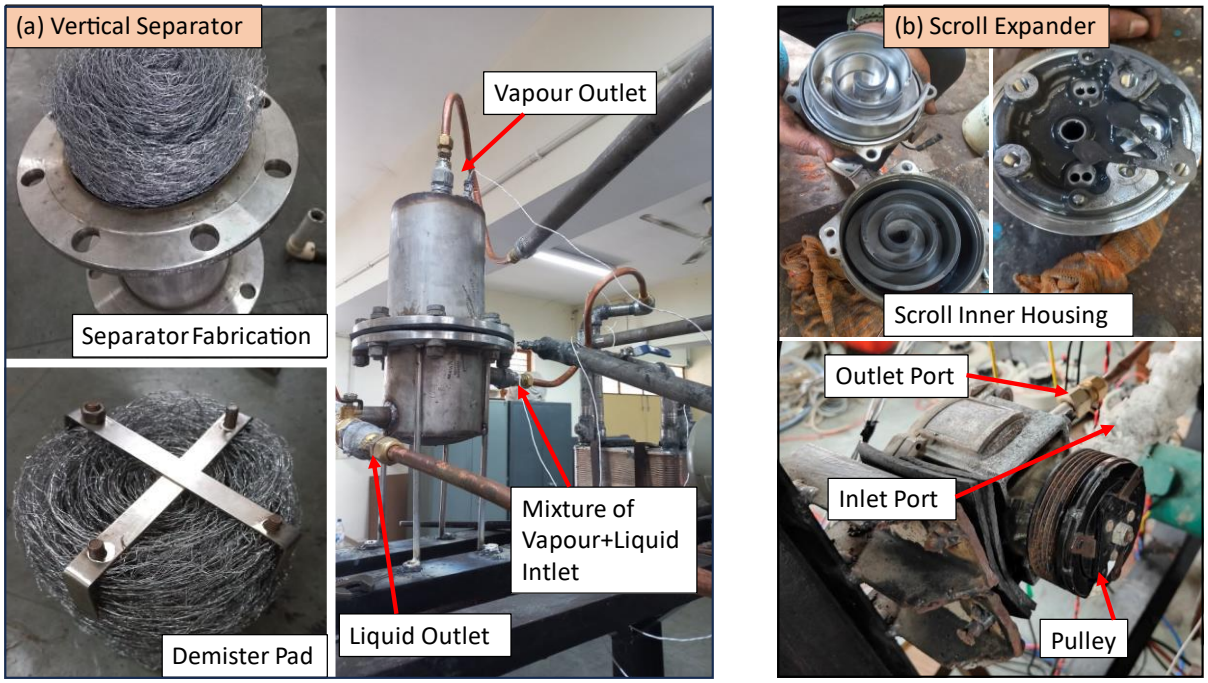


Figure 4.2. (a) Fabrication of the vertical separator and (b) modification of the scroll compressor to expander

To convert a scroll compressor into a scroll expander suitable for applications in an ORC system, several key modifications are required as shown in Figure 4.2(b). After

conducting a series of trial runs on multiple scroll compressors, the authors identified the Mitsubishi-manufactured scroll compressor from the Tata Safari automobile as the most suitable choice for the application. This selection was based on its ability to handle the required volume 90 $cm^3$, its permissible operating speed range of 1200–1600 RPM, leak-proof design, and ease of installation, which uses R134a refrigerant and polyalkylene glycol (PAG) lubricant oil in the vehicle. Modification process allows the scroll compressor to operate in reverse, expanding a high-pressure, high-temperature working fluid into a low-pressure state while generating mechanical power. The modification begins by carefully disassembling the scroll compressor to access the internal components. This step includes separating the outer casing, removing the scroll sets, and exposing the ports. Careful documentation of the original configuration can be helpful if any reassembly guidance is needed. Once disassembled, the next step is to reverse the inlet and outlet ports. Typically, a scroll compressor has an inlet and an outlet port arranged for compressing gases. For use as an expander, these ports need to be reversed: the original compressor inlet becomes the outlet for the low-pressure expanded fluid, while the original compressor outlet serves as the new high-pressure inlet. In addition to reversing the ports, it is necessary to remove the one-way (check) valve commonly found at the compressor outlet. This valve is designed to prevent reverse flow, but in the expander configuration, it would restrict the fluid's movement, which is now intended to flow in the opposite direction. By removing this valve, the modified expander allows unrestricted fluid flow from the high-pressure inlet to the low-pressure outlet. Once the primary modifications are complete, inspect the seals and bearings to ensure they are capable of withstanding the reversed flow direction as well as any increase in temperature or pressure associated with ORC applications. In some cases, it may be necessary to upgrade these components to handle the higher temperature and pressure of ORC working fluids, which can be different from those used in conventional refrigeration systems. After all necessary modifications, reassemble the scroll expander, ensuring that each component is correctly positioned and securely fastened. Applying suitable lubricants or oils for high-temperature and high-pressure environments is advisable, as ORC systems often operate with different fluids. Before full-scale deployment, the modified scroll expander should be tested under controlled conditions to confirm proper function. During this testing phase, check for any leaks, unusual sounds, or excessive vibration that could indicate issues with the modifications. If mechanical work extraction is intended, it may be beneficial to install a pulley or coupling mechanism on the expander. This setup allows the mechanical energy produced by the expansion process to drive a generator, thereby converting thermal energy into electrical power.

The three-phase heating system depicted in Figure 4.3(a) is designed for heating oil within a storage tank, using a setup that includes dual heaters, a stirrer, and variac controllers for load adjustment. Two 5-5 kW heaters are mounted on the lid of the hot oil storage tank, providing a combined heating capacity to raise the temperature of the oil efficiently. Each heater is connected to a separate 5 kW variac, allowing precise control over the input power and heat load supplied to the heaters. The use of a three-phase system is advantageous as it helps to distribute the electrical load, reducing the current in each phase and thus making the system more efficient and safer for high-power applications. Additionally, a stirrer is installed within the tank to ensure uniform mixing of the oil, promoting even temperature distribution throughout the tank and preventing hot spots. This constant stirring action enhances the heating process and ensures that the entire volume of oil reaches the desired temperature evenly. The variacs with voltage indicators allow the operator to monitor and adjust the voltage supplied to each heater independently, providing granular control over the heating intensity. A clamp meter is used to measure the current. This combination of voltage and current provides the input heat load of the heating system. This setup is crucial for applications requiring precise thermal management and is commonly used in systems where consistent, high-temperature oil is needed as a heat transfer medium.

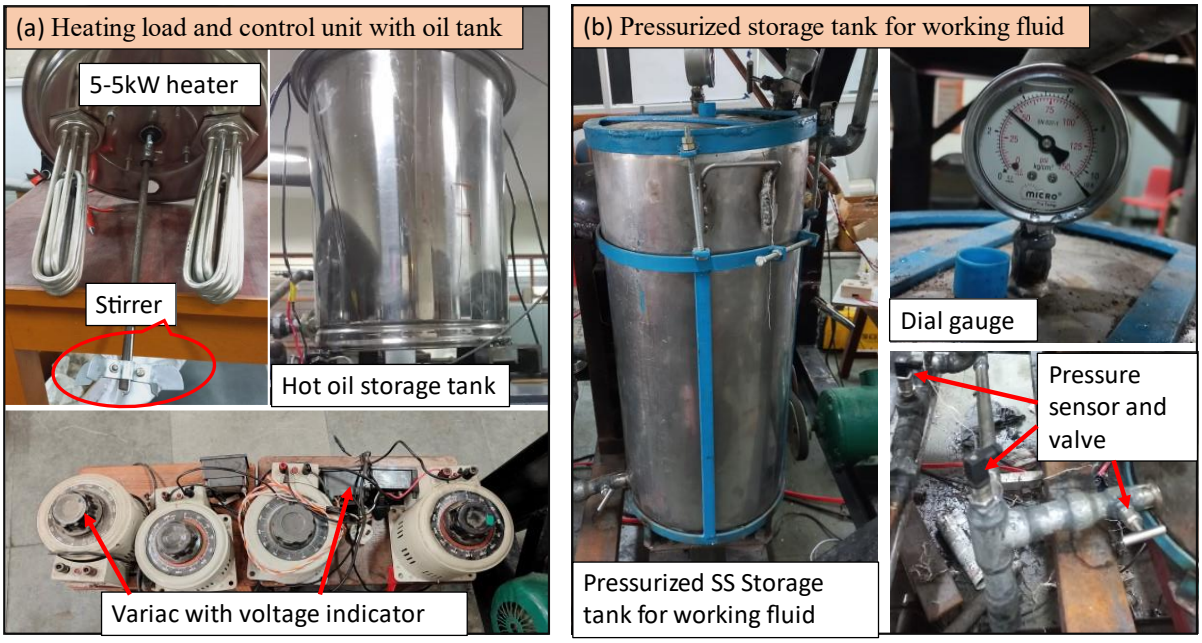


Figure 4.3. (a) Fabrication of the heating load and control unit with oil tank, (b) Pressurized storage tank for working fluid

The fabricated pressurized storage tank shown in Figure 4.3(b) is constructed from SS 314 stainless steel, designed to safely store and manage the working fluid used in the system, having 10-inch diameter and 35-inch height. The tank is equipped with three ports to facilitate the entry and exit of the circulating working fluid and to allow for the initial charging of the fluid. Each port is carefully fabricated with appropriate valves, ensuring a leak-proof design that maintains the pressurized conditions within the tank. Additionally, a pressure monitoring setup is included, with a dial gauge prominently mounted on the top for easy visibility. This dial gauge provides real-time feedback on the internal pressure levels, ensuring safe operating conditions. This robust construction ensures that the tank can handle high-pressure demands and maintain the integrity of the working fluid circulation within the system.

Other than fabricated components, ORC's main components description and technical details are tabulated in Table 4.1 for clear understanding. Table 4.1 contains the type, make, model and dimensions, along with the cost of the components.

Table 4.1. ORC component description and technical details

| **Component** | **Type** | **Make** | **Model** | **Size and Capacity** | **Cost (USD)** | **Application** |
|---|---|---|---|---|---|---|
| Evaporator | Brazed | Alfa Laval | CB40 | Heat transfer area: 1 $m^2$, Number of plates: 40 Capacity: 13.7 kw | 249.14 | Evaporation of working fluid |
| Expander | Scroll | Mitsubishi heavy industries, Purpose: Compressor of Tata Safari Storme | 5DR 2.2L VX 4X2 | Volume flow rate: 90 $cm^3$ | 973.81 | Modified to serves as turbine to generate electricity by pulley rotation |

| | | | | | | |
|---|---|---|---|---|---|---|
| Condenser | Forced air fin type | Gireesh Condensers | - | Heat transfer area: 1.7 $m^2$ | 207.14 | To condense the working fluid to liquid state |
| Pump | Hydraulic diaphragm pump with rupture detection | Grosvenor | GP-Z-C | Head: 10 $kg/cm^2$ Capacity: 1000 LPH | 1136.25 | To pump the working fluid to the evaporator |
| | Gear pump | Dhara | DP-40 | Head: 1 $kg/cm^2$ Capacity: 1500 LPH | 261.01 | To pump the hot oil to the evaporator |

#### 4.1.1.2. Instruments and Sensors

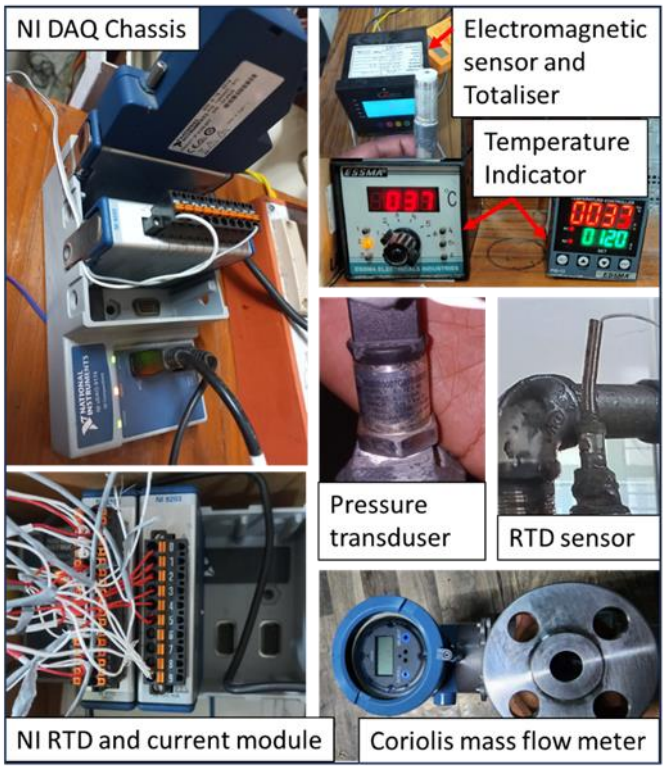


Figure 4.4. Installation of instruments and sensors to ORC setup

The instrumentation setup for the ORC experiment includes a variety of sensors and data acquisition tools that are critical for accurate measurement and data logging, as shown in Figure 4.4. An NI DAQ Chassis (National Instruments Data Acquisition System) with modules for RTD (Resistance Temperature Detector) and current measurement serves as the core for data collection. This DAQ system allows for real-time monitoring and logging of various parameters in the ORC system. The RTD sensors are used to accurately measure temperatures at different points in the system, providing crucial data for evaluating heat transfer efficiency and thermodynamic performance. A pressure transducer is installed to measure the pressure at key points, ensuring that the pressure levels are within safe operational limits and aiding in the calculation of energy transformations within the cycle. A Coriolis mass flow meter is employed for flow measurement. This sensor provides precise mass flow rate data, which is essential for balancing the thermodynamic equations and for the efficiency analysis of the ORC system. An electromagnetic sensor with a totalizer is used to measure the cumulative flow of the hot oil fluid, providing additional insights into fluid dynamics over time. Additionally, a temperature indicator is used to display temperature readings from the thermocouples placed at the entry and exit of the forced air condenser system, giving immediate feedback for on-site monitoring and adjustments. These instruments collectively enable accurate and comprehensive data collection, allowing for detailed performance analysis and optimization of the ORC system.

Table 4.2 shows the typical range and associated accuracies of the instruments used for data reduction from the ORC setup. This information is useful for analyzing the sensor's placement and accuracy in measuring the data.

Table 4.2. ORC sensors description, along with technical details

| **Sensor** | **Type** | **Make** | **Working Range** | **Accuracy** | **Position** |
|---|---|---|---|---|---|
| Pressure Transducer | Piezoelectric Type | Gem | 0-5 bar, 0-10 bar (2 nos), 0-15 bar and 0-25 bar | ±0.25% of the reading | $P_1$, $P_2$, $P_3$, $P_4$ and $P_5$ |
| Temperature Transducer | RTD | Airex | 0–850°C | ±0.2°C | $T_1$, $T_2$, $T_3$, $T_4$, $T_5$, $T_6$ and $T_7$ |

| | | | | | |
|---|---|---|---|---|---|
| | J-type | Thermonic | 0–750°C | ±1.5°C or ±0.75% of the reading | $T_8$, $T_9$ and $T_{10}$ |
| Mass Flow Meter | Coriolis | Shanghai Yinou-LZYN | 0–50 kg/min | ±0.29–2.5% of reading | Working fluid side ($\dot{m}_{wf}$) |
| Volume Flow Meter | Electromagnetic | Ztech | 25–160 lpm | ±1.5% of reading | Hot oil side ($\dot{V}_{hf}$) |
| Data Acquisition System (DAQ) | - | National Instrument | - | ±0.05% of the reading | Computer |
| Voltage and Current Meter | Clamp | Unity | 0–750V; 0–1000A | ±1% for current, ±1% for voltage | Oil Tank with Heater |

#### 4.1.1.3. Assembly of different equipment in the setup

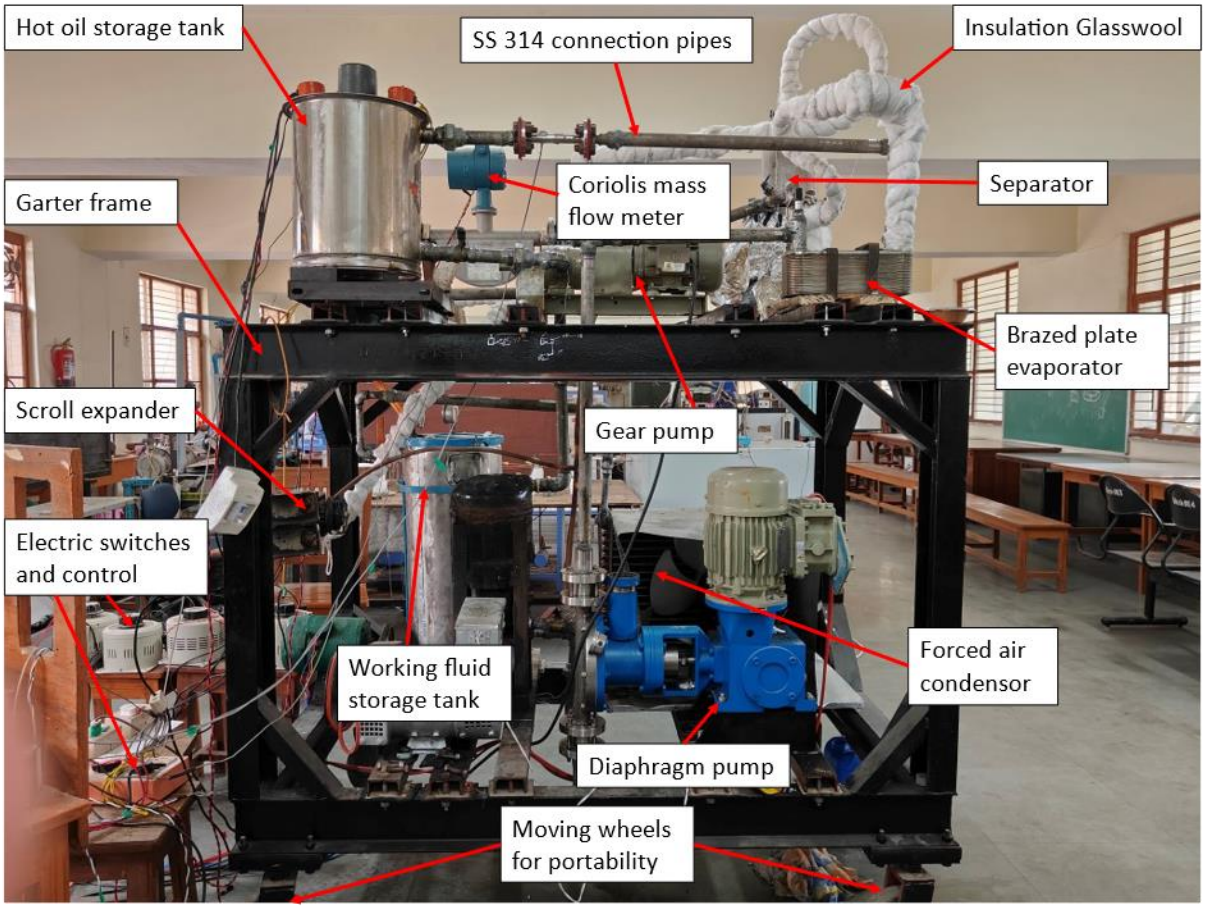


Figure 4.5. Lab-scale ORC experimental setup

The ORC experimental setup shown in Figure 4.5 consists of various components and systems assembled to enable the generation of power from low-grade thermal energy sources. The main components include a hot oil storage tank, scroll expander, working fluid storage tank, evaporator, condenser, pumps, meters, and control systems. This setup is designed to test and analyze the ORC's performance in converting thermal energy into mechanical or electrical energy. The fabrication of this ORC setup starts with building a sturdy foundation using a garter frame, typically made from steel and welded together to provide stability during operation. Moving wheels are attached to the frame base for portability, allowing the setup to be easily relocated within the laboratory or workshop. Several key components, including the hot oil storage tank, are fabricated from stainless steel (SS 314) to ensure durability and resistance to high temperatures. This storage tank is designed to store and supply thermal oil to heat the working fluid in the system. Stainless steel (SS 314) connection pipes are used to link different components, chosen for their corrosion resistance and ability to handle high temperatures. The

evaporator, designed to vaporize the working fluid by transferring heat, and the separator, which removes residual liquid from the vapor, are fabricated using SS 314 materials that can withstand high temperatures. Critical components such as the connection pipes and evaporator are wrapped with insulation glass wool to minimize heat loss, thereby improving the efficiency of the ORC system. The assembly process involves setting up a pump and flow control system, heat exchange and vaporization system, expansion and condensation system, and a control panel. The setup includes a gear pump and diaphragm pump; the gear pump circulates thermal oil from the hot oil storage tank to the evaporator, while the diaphragm pump circulates the working fluid throughout the ORC system. A Coriolis mass flow meter is placed on the working fluid line to monitor and measure the mass flow rate, which is essential for system performance analysis. In the heat exchange system, the hot oil storage tank supplies heated oil to the brazed plate evaporator, where heat is transferred to the working fluid, vaporizing it. The separator, positioned after the evaporator, ensures that only vapor enters the scroll expander. The vaporized working fluid then flows into the scroll expander, where it expands, converting thermal energy into mechanical energy. The scroll expander has been modified to operate in an expansion mode rather than compression. After expansion, the working fluid enters a forced air condenser, where it releases heat and condenses back into a liquid before returning to the storage tank. An electric control panel with switches manages the operation of pumps, flow rates, and other critical parameters, enabling precise control and safe operation during testing.
Following assembly, the ORC setup undergoes testing and calibration. A system leak test is performed on all connections, including the SS 314 pipes, pumps, and the evaporator, to ensure there are no leaks, as leaks could lead to inefficiencies and safety hazards. The Coriolis mass flow meter and control systems are calibrated to ensure accurate readings of mass flow rate and other operational parameters, enhancing the reliability of data collected during testing. The heating system, comprising the hot oil storage tank and circulation system, is tested to confirm that the thermal oil reaches the required temperature for effective heat transfer, and the effectiveness of insulation is also verified. The setup is then subjected to a trial run to assess its operational performance. During initial startup, the pumps are activated to circulate both the working fluid and thermal oil through the system, with the heated oil vaporizing the working fluid in the evaporator. This vaporized fluid is directed into the scroll expander, which begins to rotate and generate mechanical energy. Key parameters, such as mass flow rate, temperature, and pressure, are continuously monitored using the Coriolis mass flow meter and other sensors, providing essential data for evaluating the system's performance and efficiency. The condenser’s performance is observed to ensure the working fluid fully condenses before

returning to the storage tank. Data collected during the trial run is used to analyze the ORC's efficiency, heat transfer effectiveness, and the mechanical output of the expander, allowing for further adjustments and optimizations if necessary.

This experimental ORC setup provides a practical approach to harnessing low-grade heat for power generation, demonstrating the effectiveness of the ORC in converting thermal energy into mechanical energy. Through careful fabrication, assembly, testing, and operational adjustments, this setup provides valuable insights into the ORC's efficiency and effectiveness for energy conversion applications.


Figure 4.6. Isometric view and running condition of ORC experimental setup

### 4.1.2. Experimental Procedure

To conduct an experiment on the ORC setup, the following procedure has been developed, which integrates the detailed setup description, assembly, and testing process with the provided checklist instructions for startup, operation, and shutdown. Figure 4.6 shows the isometric view and running condition of the ORC experimental setup. Safety measures are emphasized throughout the process to ensure accurate data recording while avoiding accidents.

i. **Preparation and Initial Checks:** Begin by conducting a comprehensive check of the entire ORC system to ensure that all components are correctly installed and ready for operation. Inspect the garter frame for stability, and confirm that the moving wheels are locked to prevent any unintentional movement during the experiment. Carefully inspect all stainless steel (SS 314) connection pipes for any signs of leakage or weak joints, particularly at critical points around the hot oil storage tank, working fluid storage tank, gear pump, and diaphragm pump. Verify that all valves are correctly installed and can open and close smoothly.

ii. **Wiring and Electrical System:** Examine all electrical wiring and connections to the control panel and electric switches. Ensure that all wires are securely connected and safely organized to avoid contact with heated components. Put on hand gloves and a mask as an additional safety precaution before beginning any operations involving electricity or heat.

iii. **Power On and Initial System Setup:**

- Turn on the Main MCB (Main Circuit Breaker), then switch on all sensors and NI DAQ system.
- Turn on the main heater and stirrer switch to initiate uniformly heating of the oil in the hot oil storage tank. Subsequently, turn on the gear pump and open its corresponding valve to start the circulation of thermal oil towards the brazed plate evaporator.

iv. **Data Acquisition System Setup:** Connect the NI DAQ A-type cable to the computer to facilitate data logging. Run the NI code, initializing it by turning on the RTD channel and current channel within the software code. Ensure that all columns necessary for data recording, including time, heater load, hot tank temperature, hot oil mass flow rate, condenser inlet temperature, and condenser outlet temperature, are pre-set in an encoded Excel sheet and a diary to log observations manually as well.

v. **Safety Measures Before Operation:** Verify that all safety measures are in place, such as wearing hand gloves, masks and fire extinguisher, to protect against burns or inhalation of fumes. Double-check and open all valves of hot oil side and working fluid side for flow freely during the experiment.

vi. **System Start-Up:**

- Turn on the diaphragm pump and verify that its valve is open to allow fluid movement through the ORC system.
- Activate the condenser fan to ensure adequate cooling for the condensation process after expansion.

- Closely monitor the heater ampere and voltage reading to avoid overheating, and carefully observe any signs of leaks around the high-temperature areas and connections.

**vii. Data Collection and Observation:**

- As the system reaches operational temperature, data recording begins. Monitor and log all readings continuously in the Excel sheet linked to the NI system code, which captures data on temperature, pressure, and mass flow rates.
- Observe the scroll expander for any signs of abnormal vibration or noise, which may indicate issues in the expansion process.
- Ensure that all data is being correctly recorded automatically and manually to track the performance and efficiency of each component in real time.

**viii. Cautious Data Recording:**

- To avoid potential accidents, keep a safe distance from the high-temperature components like the hot oil storage tank and evaporator while observing the readings.
- Be vigilant in checking for any leaks around the piping or valves, and do not attempt to tighten or adjust any components while the system is pressurized and hot.
- Regularly inspect the condenser for proper cooling, as failure in the cooling process could result in overheating and potential hazards.

**ix. Shut Down Procedure:**

- Close the working fluid storage tank outlet valve immediately after the experiment is complete. Allow the diaphragm pump to run for an additional 0.5 minutes to circulate any remaining fluid within the system.
- Close the hot fluid valve and allow the gear pump to run for 1 minute to flush any residual hot oil, which helps in preventing leakage, overheating of the storage tank or gear pump post-operation.
- Conduct a final inspection of all connections, checking for any leaks, and ensure that all valves are securely closed.
- Turn off all switches and finally turn off the Main MCB to cut off power to the entire system.

**x. Final Data Logging and Clean-Up:** Record any final observations in the diary regarding the setup's performance, anomalies encountered, and the overall data trends observed. Save and back up the collected data from the Excel sheet to ensure no loss of information.

This ORC experiment procedure is designed to facilitate a safe and structured approach to operating and analyzing the ORC system. The startup and shutdown checklists are followed

rigorously, with particular attention to inspecting connections, monitoring leakage, and ensuring all valves and wiring are in place before initiating any heating. Data reading is carefully monitored to maintain distance from high-temperature components, and any signs of leakage are dealt with by immediately halting operations. Through this controlled procedure, the ORC setup can be tested effectively while minimizing risks and providing accurate data on the system's performance.

### 4.1.3. Data Reduction

This section details the methodology for analyzing the ORC's thermodynamic performance based on experimentally measured data. Using temperature, pressure, and flow rate data collected from the ORC setup, thermodynamic properties are required to evaluate cycle performance metrics such as heat input, work output, and thermal efficiency. The required thermodynamic equations, (2.1 - 2.19) are taken from chapter 2.

The heat input through a 3-phase heater is calculated by,

$$Q_{in} = V \times I \tag{4.1}$$

Where V is 3-phase voltage and I is current.

ORC experiment has been performed on the above setup and the data reduced is tabulated below in Table 4.3 for the mean condition of cold air inlet temperature (33°C) and volume flow rate of hot oil (50 litre/min) for different heat input loads. Table 4.3 contains all the important input and output parameters of experimental data.

Table 4.3. ORC experimental data at various heat loads and mean input condition

| **Parameter** | **Unit** | **Experimental data** | | | | |
|---|---|---|---|---|---|---|
| ***Heat Input** | (kW) | 5 | 6.5 | 8 | 10 | 11.5 |
| ***Cold air inlet temperature** | (°C) | 33.2 | 32.8 | 32.6 | 33.3 | 32.8 |
| ***Volume flow rate of hot fluid** | (litre/min) | 50.34 | 50.21 | 49.92 | 49.49 | 49.60 |
| **Pump inlet pressure** | (bar) | 1.73 | 1.75 | 1.76 | 1.76 | 1.77 |
| **Pump outlet pressure** | (bar) | 4.10 | 5.09 | 8.32 | 12.62 | 17.85 |
| **Turbine inlet pressure** | (bar) | 3.75 | 4.55 | 7.60 | 11.73 | 16.72 |
| **Turbine outlet pressure** | (bar) | 2.02 | 2.10 | 2.17 | 2.24 | 2.30 |
| **Evaporator's hot fluid inlet pressure** | (bar) | 2.06 | 2.03 | 2.06 | 2.07 | 2.07 |
| **Mass flow rate of working fluid** | (kg/sec) | 0.0053 | 0.0062 | 0.0066 | 0.0077 | 0.0079 |

| | | | | | | |
|---|---|---|---|---|---|---|
| **Hot fluid inlet temperature** | (°C) | 100.9 | 107.4 | 127.6 | 150.2 | 172.2 |
| **Hot fluid outlet temperature** | (°C) | 95.9 | 101.0 | 119.7 | 140.8 | 161.5 |
| **Pump inlet temperature** | (°C) | 34.9 | 35.0 | 34.9 | 34.8 | 35.0 |
| **Pump outlet temperature** | (°C) | 35.1 | 35.4 | 35.5 | 35.6 | 36.2 |
| **Turbine inlet temperature** | (°C) | 87.4 | 93.4 | 112.8 | 132.2 | 150.6 |
| **Turbine outlet temperature** | (°C) | 75.9 | 78.1 | 85.6 | 93.2 | 101.8 |
| **Pump isentropic efficiency** | (%) | 58.81 | 63.09 | 67.20 | 67.60 | 66.66 |
| **Turbine isentropic efficiency** | (%) | 67.75 | 71.68 | 77.27 | 80.30 | 77.05 |
| **Evaporator effectiveness** | | 0.81 | 0.81 | 0.83 | 0.83 | 0.82 |
| **Net power output** | (kW) | 0.123 | 0.189 | 0.387 | 0.670 | 0.939 |
| **Pump power** | (kW) | 0.004 | 0.005 | 0.011 | 0.018 | 0.026 |
| **Turbine power** | (kW) | 0.127 | 0.194 | 0.397 | 0.688 | 0.966 |
| **Cycle efficiency** | % | 2.34 | 2.91 | 4.75 | 6.67 | 8.08 |
| **Specific Work Output** | (kJ/kg) | 23.17 | 30.58 | 59.03 | 87.41 | 118.81 |

*Input parameters used to investigate the performance on other parameters (Table 4.3)

As the heat input increased from 5 kW to 11.5 kW, pump and turbine pressures, working fluid mass flow rate, and system temperatures rose accordingly, reflecting the system's response to higher loads. The turbine and pump pressures increased with heat input, driving higher fluid flow and power output. This was accompanied by an increase in working fluid mass flow through the evaporator. Pump and turbine isentropic efficiencies also improved, indicating better thermodynamic performance. The evaporator maintained stable effectiveness, ensuring consistent heat exchange. Net power output grew from 0.123 kW to 0.939 kW, with cycle efficiency rising from 2.34% to 8.08%, demonstrating a more efficient conversion of heat into mechanical power. Specific work output also increased, enhancing system performance under higher heat conditions. While a techno-economic analysis on a lab-scale experimental setup may not provide a precise representation of large-scale implementation, it offers valuable insights into scalability and technology validation. Considering a waste heat input of 11.5 kW, the system can generate approximately 1 kW of net power. The estimated setup costs include approximately $3,000 (₹2,60,000) for equipment, $5,500 (₹4,80,000) for instrumentation, and $1,700 (₹1,50,000) for working fluids. Assuming an annual operation of 7,000 hours, the system would produce 7,000 kWh of electricity, generating a revenue of ₹70,000 ($805) at ₹10

per kWh. Based on this, the total investment of $10,200 (₹8,90,000) can be recovered in approximately 13 years all while producing energy without burning fossil fuels.

### 4.1.4. Uncertainty Analyses

The ORC net power and cycle efficiency are primarily dependent on temperature, pressure, mass flow rates and electrical power. Each measured parameter has its own uncertainty. Using the partial derivative approach (root-sum-square method), propagate uncertainties for key calculated parameters using equation (4.2) given by (Kline and McClintock, 1953).

$$U_Z = \left[\left(\frac{\partial Z}{\partial X_1} U_{X_1}\right)^2 + \left(\frac{\partial Z}{\partial X_2} U_{X_2}\right)^2 + \cdots \ldots \ldots + \left(\frac{\partial Z}{\partial X_n} U_{X_n}\right)^2\right]^{\frac{1}{2}} \quad (4.2)$$

Where, Z is a function of the independent variables X1, X2, X3,…,Xn are the uncertainties of the independent variables. The maximum uncertainties of the calculated parameters are listed in Table 4.4.

Table 4.4. Uncertainty analyses of major input and output parameter

| **Parameters** | **Uncertainty Calculation Formula** | **Uncertainty value (%)** |
|---|---|---|
| Heat Input (kW) | $U_{Q_{in}} = \left[\left(\frac{\partial Q_{in}}{\partial V} U_V\right)^2 + \left(\frac{\partial Q_{in}}{\partial I} U_I\right)^2\right]^{\frac{1}{2}}$ | ±4.2 |
| Net Power (kW) | $U_{W_{net}} = \left[\left(\frac{\partial W_{net}}{\partial \dot{m}_{wf}} U_{\dot{m}_{wf}}\right)^2 + \left(\frac{\partial W_{net}}{\partial h_{t,i}} U_{h_{t,i}}\right)^2 + \left(\frac{\partial W_{net}}{\partial h_{t,o}} U_{h_{t,o}}\right)^2\right]^{\frac{1}{2}}$ | ±5.6 |
| Cycle Efficiency (%) | $U_{\eta_{th}} = \left[\left(\frac{\partial \eta_{th}}{\partial W_{net}} U_{W_{net}}\right)^2 + \left(\frac{\partial \eta_{th}}{\partial Q_{in}} U_{Q_{in}}\right)^2\right]^{\frac{1}{2}}$ | ±4.7 |

### 4.1.5. Optimization and Prediction

In the optimization and prediction of ORC performance, Response Surface Methodology (RSM) coupled with Analysis of Variance (ANOVA) plays a critical role. The design of experiments (DOE) through RSM enables the investigation of the relationship

between independent input variables and the response variables, such as net power output and cycle efficiency. By employing statistical models, RSM aids in optimizing performance and predicting outcomes under various conditions.

The experiments for this study were constructed using central composite design (CCD), a common approach in RSM, which allows for a systematic variation of process parameters and evaluation of their impact on the performance of the ORC. The experimental data for the ORC was derived from controlled tests and tabulated in Table 4.5, where key operating parameters such as heat load, volume flow rate of hot oil, and cold air inlet temperature were varied. The objective was to maximize both the net power output and the cycle efficiency.

Table 4.5. Design of Experiment Table by Central Composite Method

| | **Factor 1** | **Factor 2** | **Factor 3** | **Response 1** | **Response 2** |
|---|---|---|---|---|---|
| **Run** | **A: Heat Input (kW)** | **B: Cold Air Inlet Temperature (°C)** | **C: VFR of Hot Oil (litre/min)** | **Net Power (kW)** | **Cycle Efficiency (%)** |
| 1 | 11.5 | 37 | 60 | 0.864 | 7.52 |
| 2 | 5 | 37 | 40 | 0.135 | 2.70 |
| 3 | 11.5 | 29 | 60 | 0.831 | 7.23 |
| 4 | 8.25 | 33 | 40 | 0.383 | 4.64 |
| 5 | 8.25 | 33 | 50 | 0.422 | 5.12 |
| 6 | 11.5 | 33 | 50 | 0.940 | 8.17 |
| 7 | 8.25 | 33 | 50 | 0.424 | 5.14 |
| 8 | 11.5 | 37 | 40 | 0.906 | 7.88 |
| 9 | 5 | 29 | 60 | 0.092 | 1.84 |
| 10 | 5 | 37 | 60 | 0.109 | 2.18 |
| 11 | 8.25 | 33 | 50 | 0.422 | 5.12 |
| 12 | 5 | 33 | 50 | 0.123 | 2.46 |
| 13 | 5 | 29 | 40 | 0.120 | 2.39 |
| 14 | 8.25 | 33 | 50 | 0.421 | 5.11 |
| 15 | 8.25 | 33 | 50 | 0.422 | 5.11 |
| 16 | 8.25 | 33 | 50 | 0.423 | 5.12 |
| 17 | 8.25 | 33 | 60 | 0.399 | 4.84 |
| 18 | 11.5 | 29 | 40 | 0.874 | 7.60 |
| 19 | 8.25 | 29 | 50 | 0.436 | 5.28 |
| 20 | 8.25 | 37 | 50 | 0.397 | 4.81 |

The results from ANOVA were tabulated in Table 4.6, with the F-value, p-value, mean, standard deviation, adjusted $R^2$, and predicted $R^2$ provided in a structured format. Table 4.6 serves as a key tool for assessing the adequacy of the developed models and ensuring they can be used reliably for optimization.

Table 4.6. ANOVA coefficients and fit statistics of the model

| | **Response 1: Net Power** | **Response 2: Cycle Efficiency** |
|---|---|---|
| **Model** | Quadratic | Quadratic |
| **F-value** | 406.36 | 167.86 |
| **P-value** | < 0.0001 | < 0.0001 |
| **Mean** | 4.57 | 5.01 |
| **Standard deviation** | 0.2034 | 0.2193 |
| **Adjusted R2** | 0.9948 | 0.9875 |
| **Predicted R2** | 0.9789 | 0.9491 |
| **Adequate Precision** | 56.795 | 39.1257 |

The F-value tests the overall significance of the model. A higher F-value suggests that the model is significant and that the variation in the data is well-explained by the independent variables. The Model F-value for net power is 406.36 and for cycle efficiency is 167.86, which implies that the model is significant. There is only a 0.01% chance that an F-value this large could occur due to noise. The p-value indicates the probability that the observed F-value occurs by chance. P-values less than 0.0500 indicate model terms are significant. The Predicted $R^2$ is in reasonable agreement with the Adjusted $R^2$ for both responses; i.e., the difference is less than 0.2. Adequate precision measures the signal-to-noise ratio and the value greater than 4 is desirable. Thus, this model can be used to navigate the design space.

Regression equations (4.3) and (4.4) used for the prediction of net power and cycle efficiency based on the above RSM-ANOVA model are illustrated below, on heat input [A], 5-11.5 kW; cold air inlet temperature [B], 29-37 °C; and volume flow rate of hot oil [C], 40-60 litre/min. The Validity range of net power and cycle efficiency are 0.092-0.94 kW and 1.84-8.17 % respectively.

$$Net\ Power = +0.4228 + 0.3836A + 0.0058B - 0.0123C + 0.0041AB - 0.0039AC + 0.0004BC + 0.1081A^2 - 0.0069B^2 - 0.0324C^2 \quad (4.3)$$

$$Cycle\ Efficiency = +5.11 + 2.68A + 0.0753B - 0.1617C - 0.0092AB + 0.0424AC + 0.0040BC + 0.2151A^2 - 0.0542B^2 - 0.3597C^2 \quad (4.4)$$

Where A, B and C indicate independent variable Heat input, Cold air inlet temperature and Volume flow rate of hot oil, respectively.

The Predicted vs. Actual graph for ORC's net power and cycle efficiency responses in RSM-ANOVA is crucial for assessing model accuracy and shown in Figure 4.7. It compares

the model's predicted values from the regression equation as illustrated above, with actual experimental results. A strong correlation, where points align closely to the diagonal line, indicates that the model reliably captures the relationship between the input variables and the responses. Deviations from this line suggest model inaccuracies or the presence of outliers. Overall, this graph helps validate the model's predictive net power and cycle efficiency, ensuring it can be used confidently for optimization and performance forecasting of the ORC experiment setup.

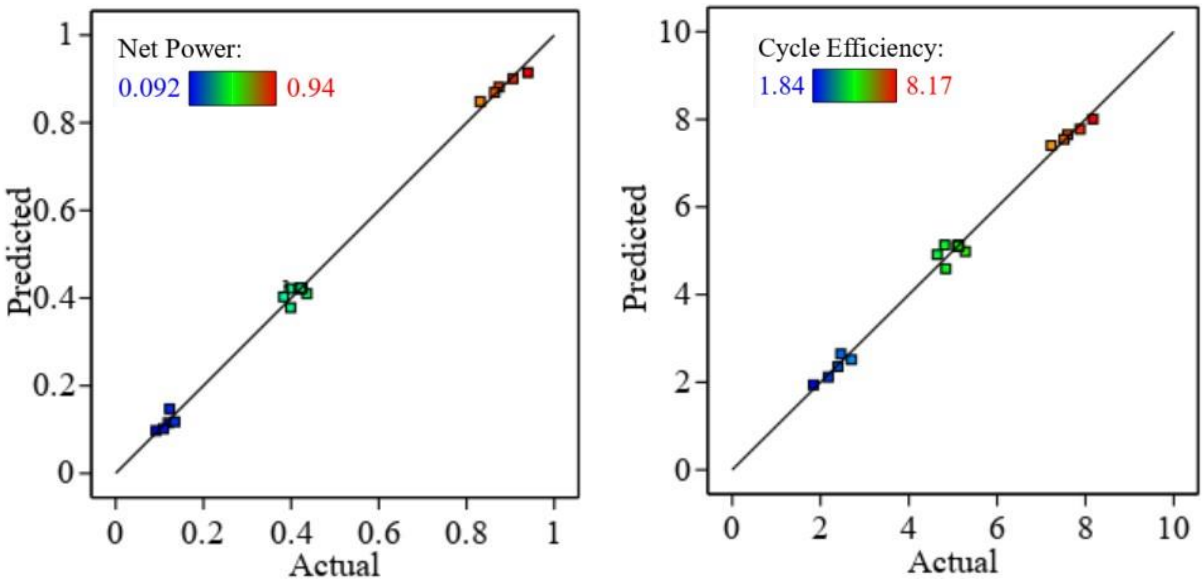


Figure 4.7. Normal plot of variation between predicted and actual value of net power and cycle efficiency

## 4.2. Results and Discussion

### 4.2.1. Effect on operating and performance parameters

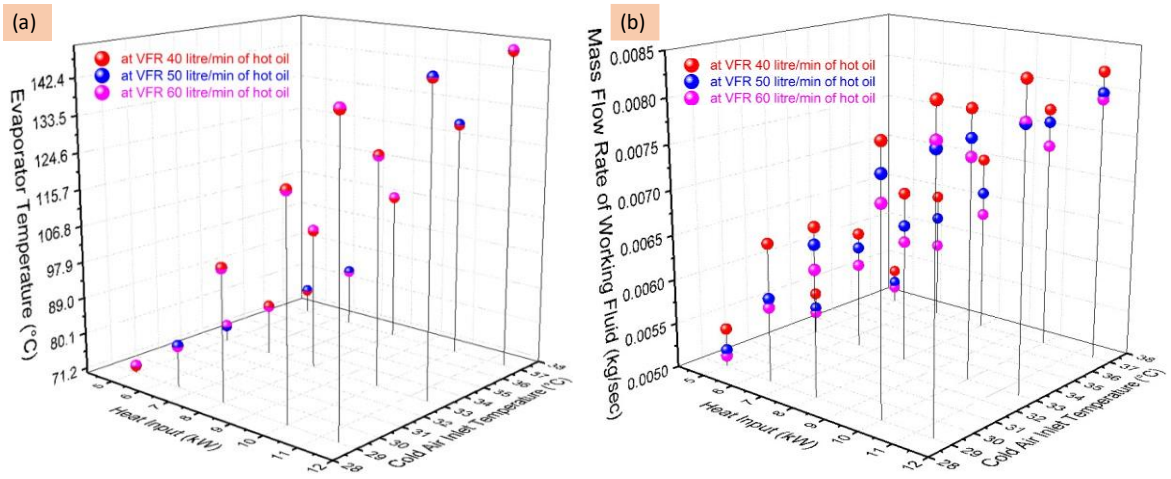


Figure 4.8. Effect on (a) Evaporator temperature and (b) Mass flow rate of working fluid

Figure 4.8(a) illustrates the relationship between heat input, VFR of hot oil, and cold air inlet temperature on the evaporator temperature in an ORC system. Data points are color-coded to indicate different VFRs, as mentioned previously, to help make a straightforward visual comparison of how variations in the hot oil flow rate impact the evaporator temperature under different conditions of heat input and cold air inlet temperatures. The plot shows a clear trend where an increase in heat input results in a corresponding rise in the evaporator temperature. This is an expected outcome, as a higher energy input elevates the thermal load in the evaporator, thus raising its temperature. Furthermore, within each level of heat input, an increase in the VFR of hot oil generally leads to a slightly higher evaporator temperature. This suggests that higher flow rates enhance the heat absorption capacity of the hot oil, improving the energy transfer efficiency in the evaporator. The VFR effect on the evaporator's temperature is not realised from the figure because of both a slight increase in the evaporator's temperature and instrument uncertainty. Additionally, the effect of cold air inlet temperature is significant in this figure. At higher cold air inlet temperatures, the evaporator temperature also tends to be higher, indicating reduced cooling effectiveness in the system. This is likely due to the decreased temperature gradient between the working fluid and the condenser air, which limits the cooling capacity and results in a warmer evaporator.

Figure 4.8(b) provides a comprehensive visualization of the relationship between the mass flow rate of the working fluid (in kg/sec) with heat input (in kW), the cold air inlet temperature (in °C) under varying VFR of hot oil in an ORC experimental setup. From the

graph, it is evident that the mass flow rate of the working fluid generally increases with a rise in both heat input and cold air inlet temperature across all tested flow rates of hot oil. For instance, at a lower heat input and colder inlet temperatures, the mass flow rate is minimal, particularly for the 60 LPM flow rate, indicating a lower thermodynamic efficiency in transferring heat to the working fluid. However, as the heat input increases, a noticeable rise in the working fluid's mass flow rate can be observed, especially at lower VFRs of 40 and 50 LPM. This trend suggests that decreasing the hot oil flow rate enhances the heat transfer capacity, thereby driving a higher mass flow rate of the working fluid in the ORC system. Moreover, the graph highlights that the impact of cold air inlet temperature on the mass flow rate becomes more pronounced at lower VFRs. This correlation indicates that a higher VFR of hot oil enhances the system's responsiveness to changes in cold air inlet temperature, likely due to improved heat exchange efficiency at elevated flow rates. Overall, the interrelationship between heat input, cold air inlet temperature, and hot oil VFR underscores the dynamic response of the ORC system under different operating conditions.

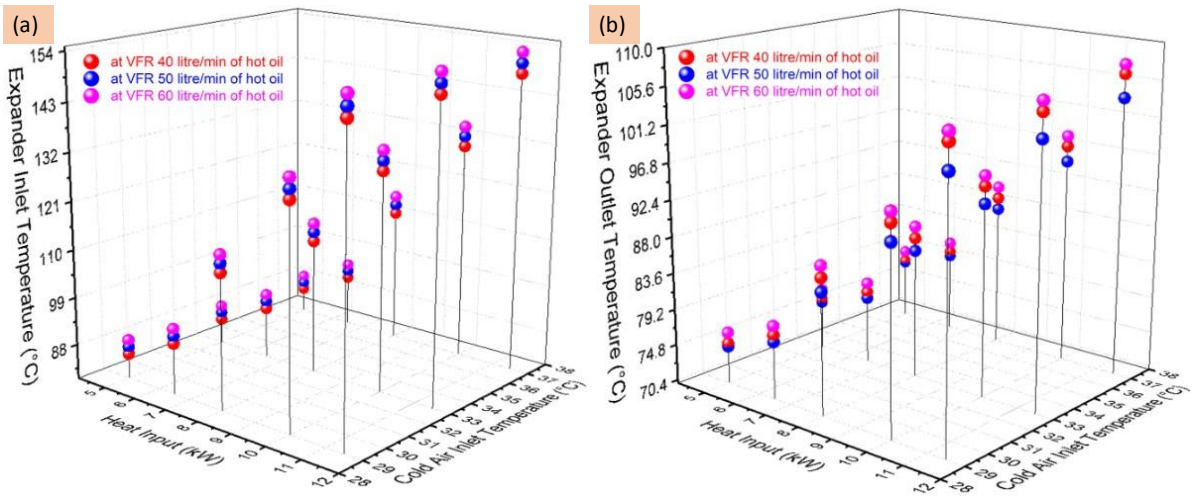


Figure 4.9. Effect on (a) expander inlet temperature and (b) expander outlet temperature

Figure 4.9(a) illustrates the expander inlet temperature variations against the heat input, cold air inlet temperature, and different volumetric flow rates of hot oil (40, 50, and 60 liters per minute). As the heat input increases, a corresponding increase in the expander inlet temperature is observed, which is consistent across all volumetric flow rates. This trend suggests that the heat input plays a dominant role in raising the working fluid's temperature before it enters the expander, thereby contributing directly to the system's thermal efficiency. At each heat input level, the expander inlet temperature also exhibits a slight variation based

on the cold air inlet temperature, implying a secondary effect where lower cold air temperatures might allow better heat retention in the system. However, the effect of varying the volumetric flow rate of hot oil is more pronounced. For instance, at higher flow rates (60 litres per minute), the expander inlet temperature reaches slightly higher values compared to lower flow rates (40 litres per minute), suggesting that increased flow rates enhance the heat transfer process, allowing more heat to be absorbed by the working fluid.

Figure 4.9(b) graph shows the expander outlet temperature as a function of the same parameters: heat input, cold air inlet temperature, and varying flow rates of hot oil. Similar to the inlet temperature behaviour, the outlet temperature also rises with an increase in heat input. However, the difference between the inlet and outlet temperatures at each flow rate and heat input provides insight into the expander's effectiveness in extracting work from the working fluid. A notable observation is that at higher volumetric flow rates, the outlet temperature tends to be higher, indicating that the expander releases less heat under these conditions. This behaviour could imply that at elevated flow rates, the working fluid has less residence time within the expander, resulting in a lower degree of expansion and heat extraction. Conversely, at lower flow rates (40 litres per minute), the working fluid undergoes a more extensive expansion, leading to a lower outlet temperature, which could be more favourable for work extraction efficiency in certain ORC configurations.

The heat input primarily drives the inlet temperature, which subsequently influences the outlet temperature depending on the flow rate and cooling conditions. Increased flow rates generally lead to higher inlet and outlet temperatures, potentially maximizing the ORC's thermal output at the expense of expansion effectiveness. On the other hand, optimizing the flow rate at each heat input level can enable better control over the expander's thermal and mechanical output, leading to potentially improved efficiency.

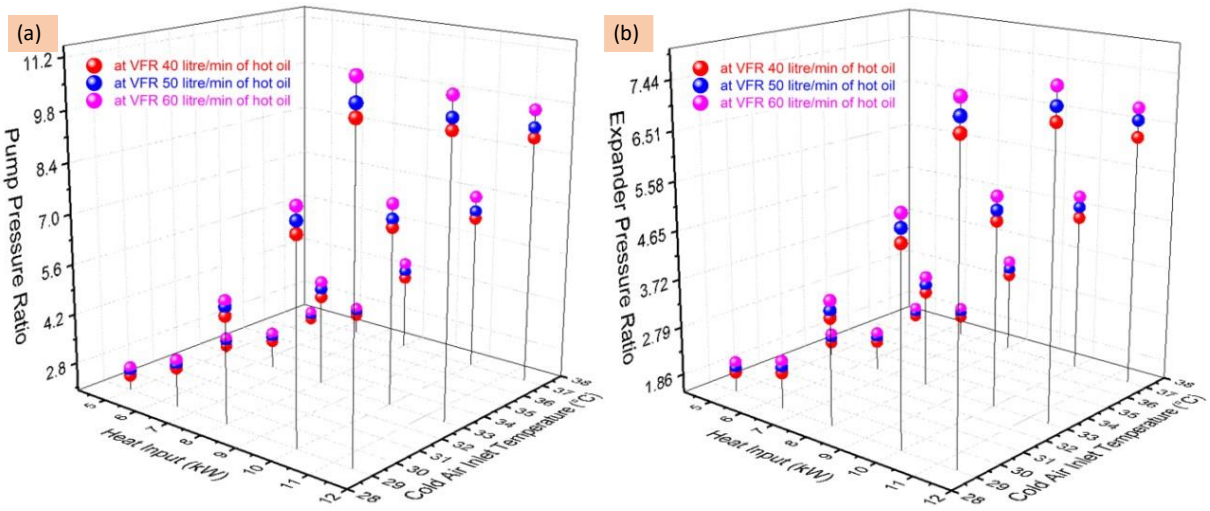


Figure 4.10. Effect on pressure ratio of (a) pump and (b) expander

Figure 4.10(a) illustrates the pump pressure ratio as it varies with heat input, cold air inlet temperature, and different VFRs of hot oil. The pump pressure ratio, representing the pressure increase across the pump, is a critical factor for ensuring the effective circulation of the working fluid. The graph shows that the pump pressure ratio increases as the heat input increases. This trend is logical because a higher heat input results in a greater thermal energy input to the working fluid, elevating its vapour pressure. As a result, the pump needs to operate at a higher pressure ratio to maintain circulation. Interestingly, the pump pressure ratio decreases with an increase in the inlet temperature of cold air. This inverse relationship may be due to the reduced cooling effect at higher cold air temperatures, which leads to a slightly higher temperature of the working fluid exiting the condenser. The volumetric flow rate of hot oil also affects the pump pressure ratio. At a higher VFR (e.g., 60 litres per minute), the pump pressure ratio is generally higher at each level of heat input and cold air temperature. This is because a higher hot oil flow rate improves heat transfer to the working fluid, raising its vapour pressure at the pump inlet. Consequently, the pump requires a higher pressure ratio to drive the fluid through the cycle effectively.

Figure 4.10(b) illustrates the expander pressure ratio under different conditions of heat input, cold air inlet temperature, and hot oil flow rate. The expander pressure ratio is critical for converting thermal energy into mechanical work and reflects the difference in pressure across the expander. Similar to the pump pressure ratio, the expander pressure ratio increases with higher heat input. This behaviour is expected as more heat input raises the pressure of the vapor entering the expander, thereby increasing the pressure ratio across it. Notably, the expander pressure ratio also decreases with an increase in the cold air inlet temperature. This

trend occurs for similar reasons as seen in the pump pressure ratio. With a higher inlet temperature of cold air, the condenser's cooling efficiency is reduced, leading to a higher outlet temperature of the working fluid from the condenser. This results in lower condensation pressure, thereby reducing the overall pressure differential across the expander and subsequently the expander pressure ratio. The volumetric flow rate of hot oil has a pronounced impact on the expander pressure ratio as well. Higher flow rates, such as 60 litres per minute, lead to increased expander pressure ratios across all levels of heat input and cold air inlet temperatures. This is due to enhanced heat transfer from the hot oil, which elevates the working fluid's pressure at the expander inlet. Thus, a higher hot oil flow rate increases the pressure difference across the expander, enhancing the potential for mechanical work extraction.

Increasing heat input positively impacts both pump and expander pressure ratios, which is beneficial for energy conversion efficiency. However, the cold air inlet temperature should ideally be kept low to maintain high pressure differentials across both the pump and the expander. Lower cold air inlet temperatures improve condensation efficiency, which helps sustain higher pressure ratios in the system and ultimately enhances the overall cycle efficiency. The volumetric flow rate of hot oil is another critical parameter. A higher VFR improves heat transfer, leading to increased pressure ratios, especially under higher heat inputs. However, it is essential to manage the flow rate to ensure the system operates within safe pressure limits.

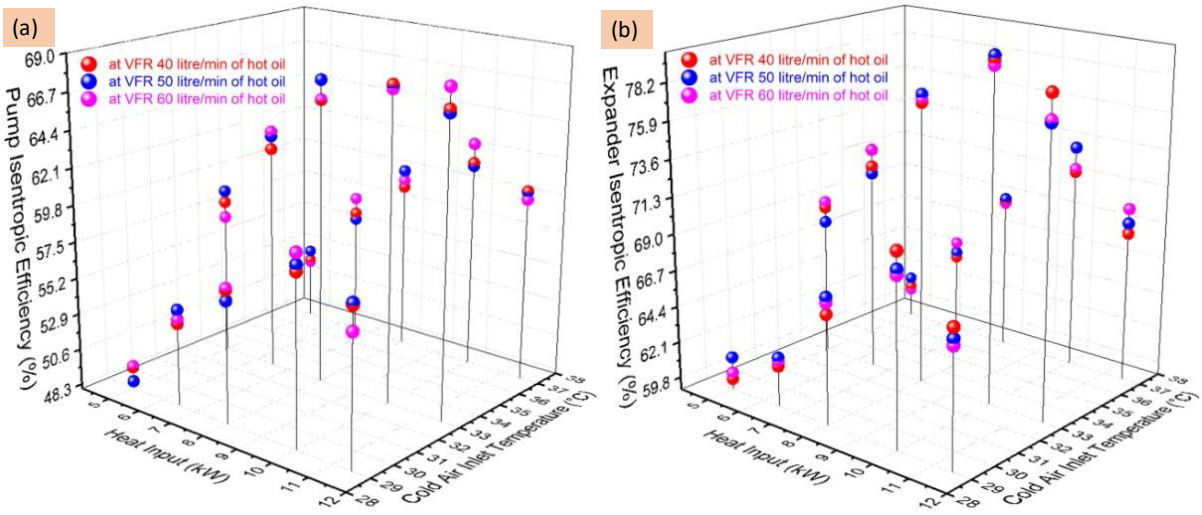


Figure 4.11. Effect on isentropic efficiency of (a) pump and (b) expander

Figure 4.11(a) illustrates the interrelationship between various parameters affecting the isentropic efficiencies of the pump in an ORC system. Specifically, these 3D plots display the pump and expander isentropic efficiencies as functions of heat input and cold air inlet

temperature, with data segmented by VFR of the hot oil at 40, 50, and 60 litres per minute. In the first plot, which represents the pump's isentropic efficiency, it can be observed that at lower heat inputs (5–10 kW), the efficiency generally remains lower and shows minor variations with changes in air inlet temperature. As the heat input increases, the pump's isentropic efficiency becomes more sensitive to the air inlet temperature, particularly at higher flow rates of 50 and 60 litres per minute. This relationship indicates that under higher heat input conditions, the performance of the pump improves as the system handles increased thermal energy more effectively.

Figure 4.11(b), depicting the expander's isentropic efficiency, shows a similar trend with a stronger correlation between higher heat input and efficiency improvements. However, the expander efficiencies are notably higher than those of the pump across the heat input range, particularly at the highest flow rate (60 litres per minute). This suggests that the expander performs more optimally under elevated thermal loads and increased flow rates, likely due to enhanced working fluid expansion under these conditions. The expander's efficiency also demonstrates greater responsiveness to variations in air inlet temperature, emphasizing the role of cooling efficiency in maintaining optimal performance.

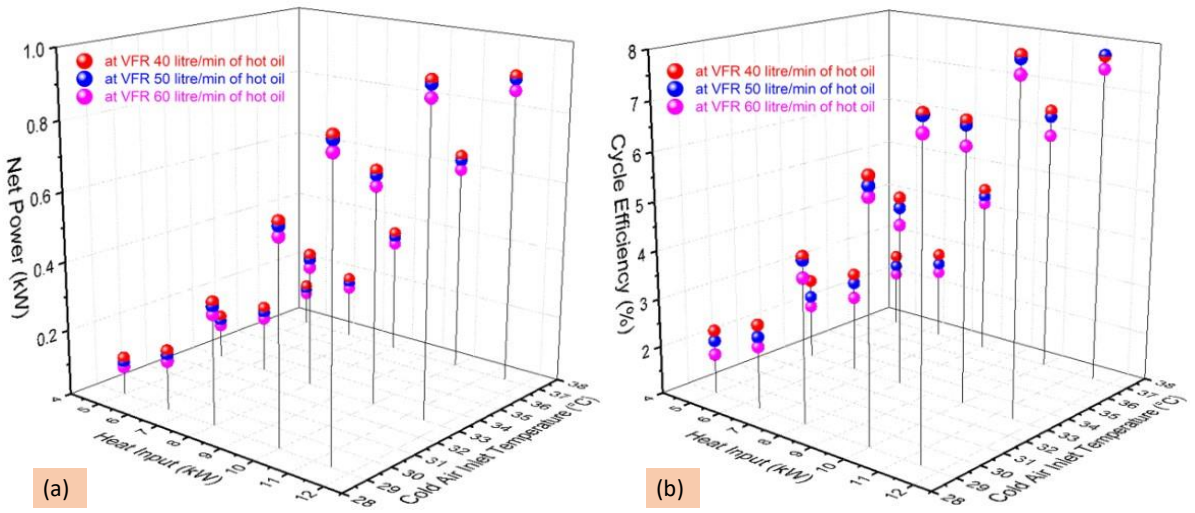


Figure 4.12. Effect on (a) net power output and (b) cycle efficiency

Figure 4.12 illustrates the interrelationships between heat input (kW), cold air inlet temperature (°C), and volumetric flow rates (VFR) of hot oil (40, 50, and 60 LPM) on two key performance parameters in the ORC system: net power output (kW) and cycle efficiency (%). These parameters are critical for evaluating the thermodynamic performance of the ORC system under various operating conditions. Figure 4.12(a) presents the net power output of the

ORC system as a function of heat input and cold air inlet temperature at each of the three tested hot oil flow rates. A clear trend is observed, where an increase in heat input and cold air inlet temperature generally corresponds to an increase in net power output across all flow rates. For example, at lower heat inputs and colder air temperatures, the net power output is relatively low for all VFR levels, indicating limited energy conversion. However, as the heat input rises, a more significant increase in net power output is seen, especially for higher VFRs (50 and 60 LPM). This suggests that greater flow rates of hot oil enhance the heat transfer effectiveness, enabling the working fluid to extract more thermal energy and convert it into mechanical power. Notably, the net power output at 60 LPM reaches peak values at high heat input levels, confirming that increased VFR contributes to higher net power outputs under optimal thermal conditions.

Figure 4.12(b) displays the cycle efficiency, which is similarly influenced by heat input, cold air inlet temperature, and hot oil VFR. Here, the ORC efficiency follows a trend similar to that observed in net power output, with efficiency increasing alongside higher heat inputs and warmer air inlet temperatures. However, a distinct observation is that the impact of VFR on cycle efficiency appears to be more complex. At lower heat inputs, the cycle efficiency is relatively comparable across all flow rates, suggesting the limited influence of VFR on efficiency under low thermal conditions. As heat input increases, however, a divergence in efficiency emerges, with the highest cycle efficiency values observed at the 40 LPM flow rate. This indicates that, beyond a certain threshold, higher VFRs may not proportionally increase efficiency due to increased parasitic losses associated with pumping and thermal resistance.
Both graphs offer valuable insights into the performance dynamics of the ORC system. They reveal that while increased VFR of hot oil enhances net power output, optimal cycle efficiency may be achieved at moderate flow rates under high heat inputs, indicating a trade-off between maximizing power output and achieving thermal efficiency. This analysis provides essential guidelines for selecting appropriate operational parameters in ORC systems to balance power generation and energy efficiency based on specific application requirements.

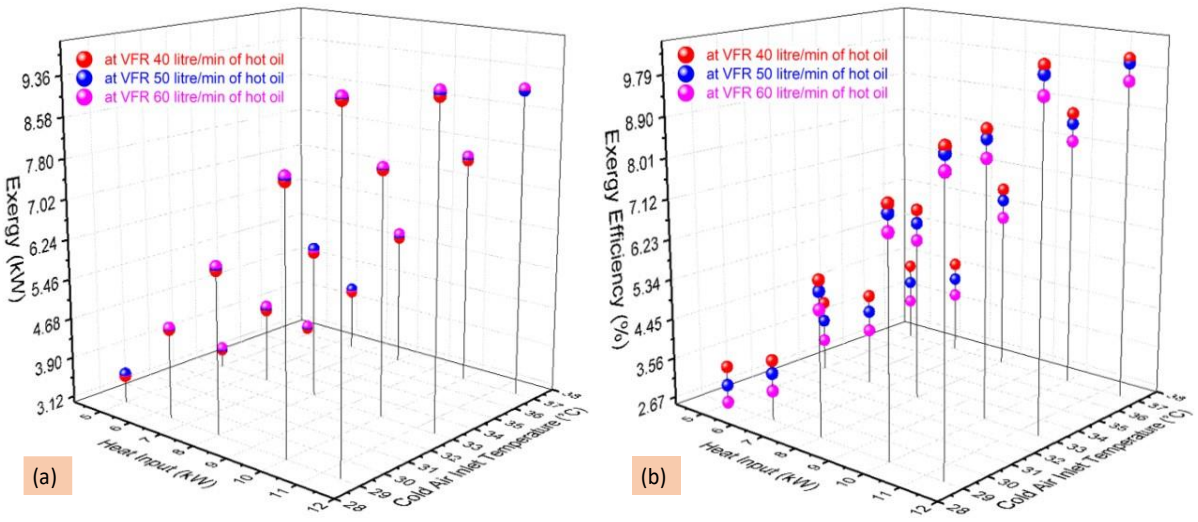


Figure 4.13. Effect on (a) exergy and (b) exergy efficiency

Figure 4.13 illustrates the influence of heat input, cold air inlet temperature, and the VFR of hot oil on the exergy and exergy efficiency. In Figure 4.13(a), the exergy (kW) is plotted against heat input (kW) and cold air inlet temperature (°C) for three different VFRs of hot oil: 40, 50, and 60 L/min. As observed, the exergy output increases with rising heat input, regardless of the VFR. This trend suggests that higher thermal energy input directly enhances the exergy available for conversion, likely due to an improved temperature gradient across the ORC system. Additionally, at a constant heat input, higher cold air inlet temperatures tend to result in a marginally lower exergy output. This effect could be attributed to reduced thermal efficiency at elevated condenser temperatures, limiting the potential for work extraction.

In Figure 4.13(b), the exergy efficiency (%) is plotted similarly against heat input and cold air inlet temperature for the three VFR levels. The results show that exergy efficiency improves with increasing heat input across all flow rates. This efficiency gain is primarily due to enhanced system performance under higher energy availability, which allows more effective utilization of the working fluid's thermodynamic potential. Notably, lower VFRs (e.g., 40 L/min) tend to yield slightly higher exergy efficiencies than higher VFRs at comparable conditions. This observation may be explained by the reduced heat transfer losses at lower flow rates, which improves overall energy utilization efficiency.

These graphs demonstrate that optimizing heat input and controlling the VFR of hot oil are essential for enhancing both exergy and exergy efficiency in ORC systems. Elevated heat input levels promote higher exergy outputs and efficiencies, while a moderate flow rate may be preferable for achieving optimal exergy efficiency. These findings provide valuable insights

into the operational parameters that can maximize ORC performance under varying conditions, paving the way for more efficient waste heat recovery in practical applications.

### 4.2.2. ANOVA model for optimization and prediction

The following constraints were taken into consideration while ORC's experimental data is being optimized by the RSM-ANOVA method for maximum net power and cycle efficiency. Equal weightage is given to both factors as the condition is described in the following Table 4.7. Independent variables A, B and C is being tested for all its range to find the optimum condition of A, B and C at which both net power and cycle efficiency is maximum.

Table 4.7. ANOVA optimization constraints

| Name | Goal | Lower Limit | Upper Limit | Lower Weight | Upper Weight | Importance |
|---|---|---|---|---|---|---|
| A: Heat Input (kW) | is in range | 5 | 11.5 | 1 | 1 | 3 |
| B: Cold Air Inlet Temperature (°C) | is in range | 29 | 37 | 1 | 1 | 3 |
| C: VFR of Hot Oil (litre/min) | is in range | 40 | 60 | 1 | 1 | 3 |
| Net Power (kW) | maximize | 0.092 | 0.940 | 1 | 1 | 3 |
| Cycle Efficiency (%) | maximize | 1.843 | 8.170 | 1 | 1 | 3 |

Functions with the highest desirability are selected to maximize both the net power and cycle efficiency. Desirability plays a crucial role in optimizing net power and cycle efficiency in RSM-ANOVA by providing a single metric to balance multiple responses, as shown in Figure 4.14. It translates both objectives, maximizing net power and cycle efficiency, into a scale between 0 (undesirable) and 1 (most desirable). By combining these desirability, the optimization process identifies operating conditions that achieve the best overall system performance, ensuring an effective trade-off between the competing responses. This helps to find the optimal settings for maximization of both power output and cycle efficiency simultaneously by heat input, cold air inlet temperature, and VFR of hot oil.

Figure 4.14 illustrates the desirability analysis, shown at the top, which measures how well the selected parameter values satisfy both objectives. The highest heat input value of 11.5 kW significantly increases net power output and cycle efficiency, with a near-perfect desirability of 0.978, indicating that this heat input is optimal for system performance. At this input, net power reaches 0.92 kW, and cycle efficiency climbs to 8.037%, reflecting the

system's improved energy conversion efficiency. On the other hand, the cold air inlet temperature, optimized at 35.611°C, and the hot oil VFR at 48.031 litre/min, show a relatively flat response in terms of desirability. This suggests that these two parameters are less sensitive to variations and have a minor influence on improving performance compared to heat input. The flat curves in these two plots indicate that slight deviations from their optimal points may not drastically affect system performance, unlike heat input, which plays a more dominant role.

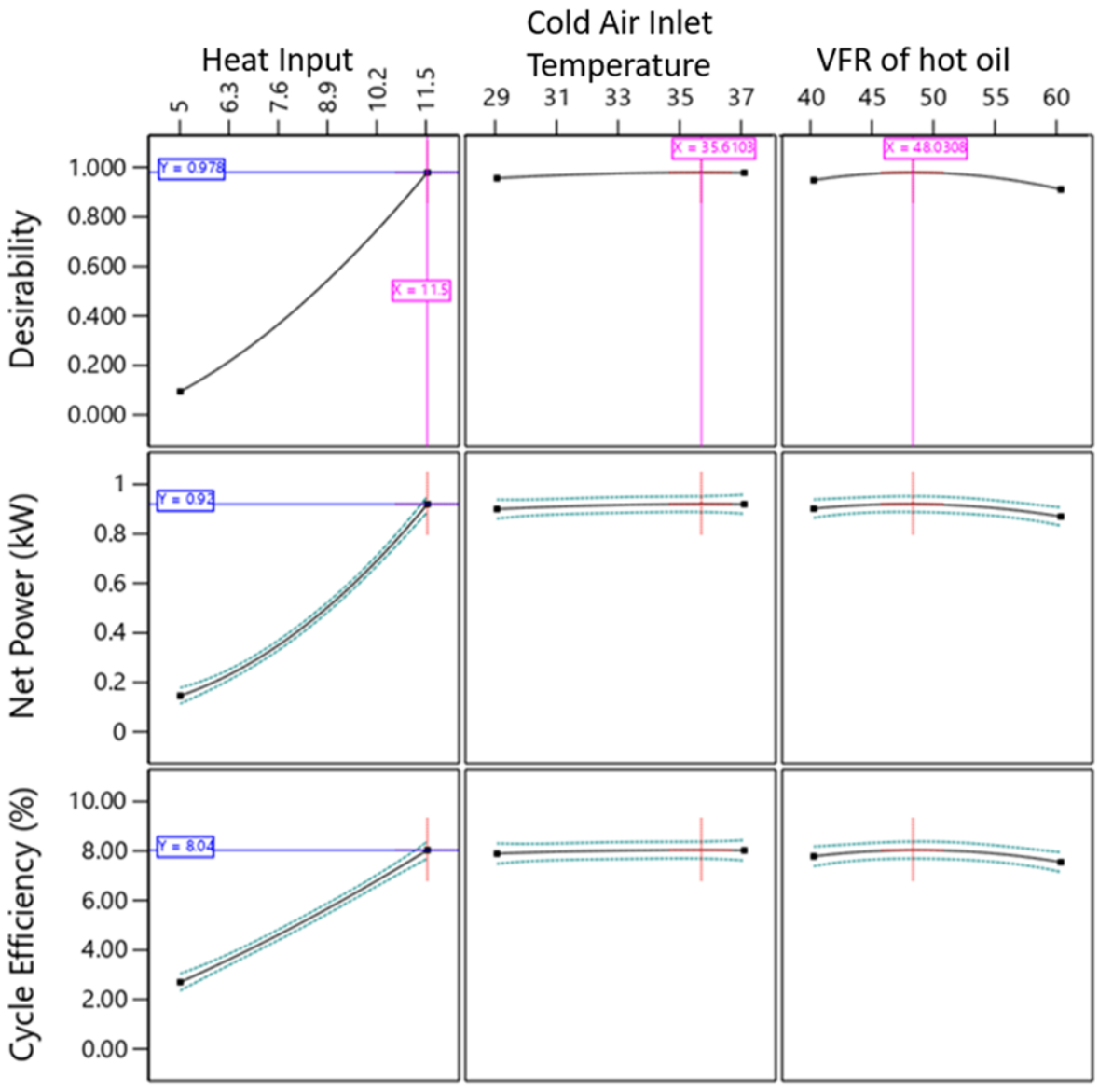


Figure 4.14. Desirability for net power and cycle efficiency for prediction analysis

Table 4.8 presents the optimized conditions for the independent variables heat input, cold air inlet temperature, and VFR of hot oil that achieves a balance between maximizing net power output and cycle efficiency. These optimized settings were validated through experimental

testing under nearly identical conditions. The heat input was set to 11.5 kW, with a cold air inlet temperature of 35°C, and a VFR of hot oil at 48 litre/min. In the experimental test run, the actual net power output was found to be 0.906 kW, which is close to the optimized prediction of 0.920 kW, resulting in a minor error of 1.55%. Similarly, the experimental cycle efficiency was 7.878%, compared to the predicted 8.037%, with an error of 2.01%. These small discrepancies between the optimized and actual values are within acceptable limits, demonstrating that the model's optimization is reliable and accurate. The low error percentages confirm the effectiveness of the optimization process in predicting real-world ORC system performance under the given conditions.

Table 4.8. Validation of optimized condition output result with the experimental run at same optimized condition

| | | Optimized | Test Run | Error (%) |
|---|---|---|---|---|
| Independent Variable | Heat Input (kW) | 11.5 | 11.5 | - |
| | Cold Air Inlet Temperature (°C) | 35.611 | 35 | - |
| | VFR of Hot Oil (litre/min) | 48.031 | 48 | - |
| Dependent Variable | Net Power (kW) | 0.920 | 0.906 | 1.55 |
| | Cycle Efficiency (%) | 8.037 | 7.878 | 2.01 |

Table 4.9 presents predicted data for net power and cycle efficiency in an ORC system, highlighting both experimental and theoretical predictions. The analysis considers key input parameters heat input (kW), cold air inlet temperature (°C), and the VFR of hot oil (litre/min) to assess their impact on system performance, with statistical calculations performed at a 95% confidence level, 99% population coverage, and a tolerance level of 0.99. The model incorporates a standard deviation of 20.34 for net power and 0.22 for cycle efficiency, which offers insight into the variability of these outputs under the specified experimental conditions. For the first five rows, predictions for net power and cycle efficiency are generated based on specific input parameters, such as heat input, cold air inlet temperature, and VFR of hot oil, and validated through simultaneous test runs to observe prediction error. In these rows, prediction accuracy improves at higher heat inputs, as evidenced by the lower error values, which indicates reliable model performance in these conditions. For instance, at a heat input of 11.5 kW and 50 LPM (S.N. 5), the predicted mean was 0.917 kW, close to the observed 0.864 kW, showing a -6.15% prediction error. Cycle efficiency also follows this trend, with minimal error between predicted and observed values, particularly at moderate to high heat inputs and VFRs, indicating stable predictive accuracy. Several entries (S.N. 6–10) lack observed values, providing useful benchmarks for future validation. These cases demonstrate the model's

potential to predict system performance under varied conditions. The data suggests that the model is more accurate at higher heat inputs irrespective of cold air inlet temperatures and VFRs, making it a valuable tool for further outcome predictions under high thermal load. This analysis confirms the model's robustness, especially for high heat input scenarios, and its utility for optimizing ORC performance across diverse operating conditions.

Table 4.9. Predicted data for net power and cycle efficiency in an ORC system, highlighting both experimental and theoretical predictions

| | **Input Parameters for Predictions** | | | **Predicted Response 1: Net Power (kW)** | | | | **Predicted Response 2: Cycle Efficiency (%)** | | | |
|---|---|---|---|---|---|---|---|---|---|---|---|
| **S. N.** | **A: Heat Input (kW)** | **B: Cold Air Inlet Temp (°C)** | **C: VFR of Hot Oil (litre/min)** | **Predicted Value** | **Standard Error of Prediction** | **Observed Value** | **Prediction and Observed Error (%)** | **Predicted Value** | **Standard Error of Prediction** | **Observed Value** | **Prediction and Observed Error (%)** |
| 1. | 5 | 33 | 40 | 0.123 | 0.018 | 0.137 | 10.15 | 2.49 | 0.2 | 2.75 | 9.45 |
| 2. | 8.25 | 29 | 60 | 0.365 | 0.018 | 0.411 | 11.18 | 4.46 | 0.2 | 4.93 | 9.53 |
| 3. | 10 | 33 | 50 | 0.661 | 0.01 | 0.671 | 1.49 | 6.62 | 0.11 | 6.71 | 1.34 |
| 4. | 10 | 37 | 60 | 0.616 | 0.018 | 0.611 | -0.70 | 6.14 | 0.19 | 6.11 | -0.49 |
| 5. | 11.5 | 37 | 50 | 0.917 | 0.018 | 0.864 | -6.15 | 8.02 | 0.2 | 7.52 | -6.65 |
| 6. | 6 | 36 | 45 | 0.204 | 0.012 | - | - | 3.39 | 0.13 | - | - |
| 7. | 7 | 34 | 54 | 0.282 | 0.01 | - | - | 4 | 0.11 | - | - |
| 8. | 9 | 32 | 40 | 0.496 | 0.016 | - | - | 5.51 | 0.17 | - | - |
| 9. | 10 | 35 | 55 | 0.648 | 0.011 | - | - | 6.48 | 0.11 | - | - |
| 10. | 11 | 30 | 50 | 0.814 | 0.014 | - | - | 7.45 | 0.15 | - | - |

Table 4.10. Advantages of current developed system with previously developed systems

| Criteria | This Study | Previous Studies |
|---|---|---|
| Working Fluid & Cycle Configuration | R601a (Isopentane) – Experimentally validated, operated with a saturated vapor inlet for maximum power output | Mostly R123, R245fa, R134a, with a focus on superheated ORC, which results in lower power output at the same pressure [32,67,77,86–88] |

| | | |
|---|---|---|
| Expander & Component Innovation | Modified scroll compressor as an expander; custom-built separator for saturated vapor condition | Scroll, screw, rolling piston, and turbo expanders; no reported use of a dedicated separator [29,30,35,37,60,66,71,74,75,77] |
| Optimization & Validation | RSM-ANOVA used for performance prediction and optimization, validated with minimal error (1.55% for power, 2.01% for efficiency) | No prior ORC study optimized conditions using RSM-ANOVA; limited optimization studies focused on individual parameters [63,81] |
| Experimental Parameters & Operating Conditions | Simultaneous variations in heat input (5–11.5 kW), cold air inlet temperature (29–37°C) and volume flow rate of hot oil (40–60 LPM), | Most studies varied only one or two parameters; experiments generally conducted below 10 kW heat input [29,30,32,40,60,88,89] |
| Performance (Net Power & Efficiency) | Maximum net power: 0.939 kW, Maximum thermal efficiency: 8.08% | Power output: 0.3 – 2.5 kW, Efficiency: 3–7% [32,37,74,86–89] |
| Application Scope | Suitable for waste heat recovery from 95–180°C sources, including geothermal, solar collectors, and industrial waste heat | Mostly focused on specific temperature ranges and applications [29,40,60,80] |

Table 4.10 shows the advantages and comparison of this manuscript ORC experimental setup with previous developed ORC systems. This experimental setup provides maximum thermal efficiency that no one has achieved so far due to novel R601a working fluid and operating condition. This ORC system is designed to operate with any waste heat source within a temperature range of 95–180 °C. As such, it is well-suited for applications including geothermal energy recovery, solar collector systems, industrial waste heat utilization, and the harnessing of exhaust heat. The ORC system faces limitations in utilizing nanofluid-based novel working fluids because the existing heat exchanger design requires significant modifications. Additionally, adapting large-scale scroll expanders from standard scroll compressors presents challenges for small-scale production. These obstacles could be overcome with further design optimizations and economies of scale in a commercial application.

## 4.3. Important Findings

The experiments have been performed on the fabricated lab-scale basic ORC system to analyze the thermal performance, which is a significant parameter in generating electricity. The input parameter heat load is varied from 5kW to 11.5kW, cold air inlet temperature is varied from 29°C to 37°C and the volume flow rate of hot fluid (oil) is varied from 40 litre/min to 60 litre/min. The variation effect of input parameters in being analyzed on systems temperature, pressure and mass flow rate. The following outcomes are deduced from the results.

(i) Increased heat input positively influenced both net power output and cycle efficiency. As heat input rose from 5 to 11.5 kW, net power significantly increased, reaching a peak of 0.939 kW, while cycle efficiency improved from 2.34% to 8.08%.

(ii) Optimal cycle efficiency was achieved at the highest heat input of 11.5 kW and moderate volume flow rates, suggesting that increasing VFR beyond a certain point can diminish efficiency gains due to parasitic losses.

(iii) Exergy output increased with higher heat inputs, as more thermal energy provided a greater potential for conversion. However, the exergy efficiency was highest at moderate flow rates (e.g., 40 litre/min), as excessive flow rates reduced energy utilization efficiency due to higher heat losses.

(iv) Cold air inlet temperature inversely impacted exergy output, as elevated condenser temperatures reduced the cooling gradient, limiting work extraction potential.

(v) Evaporator effectiveness ranged from 0.78 to 0.84, with improved efficiency at higher heat inputs and VFRs of hot oil, showcasing the system's enhanced heat transfer capability.

(vi) The expander demonstrated optimal isentropic efficiency under high thermal load, with notable performance improvements at elevated VFRs due to increased fluid expansion.

(vii) Mass flow rate of the working fluid rose with higher heat inputs and cold air inlet temperatures, particularly at low VFRs, where heat transfer was maximized.

(viii) The optimization achieved using Response Surface Methodology (RSM) and Analysis of Variance (ANOVA) was validated by experiments, showing low error margins (e.g., 1.55% for net power and 2.01% for cycle efficiency), confirming model accuracy.

(ix) Desirability analysis confirmed that maximizing heat input had the greatest impact on performance, while adjustments in cold air inlet temperature and hot oil VFR had smaller effects. This suggests that, while important, these parameters can vary slightly without significantly affecting performance, whereas optimizing heat input is crucial.

Experiment working prototype setup Video link (drive):
*https://drive.google.com/file/d/1Yx6cehR4Ft3RagchZ2eJOHpyopIi-Rk7/view?usp=drive_link*.